Analyst

Accepted Manuscript

This article can be cited before page numbers have been issued, to do this please use: M. Wang, C. Ye, S. BAO, Y. Zhang, Y. Yu and M. Xu, *Analyst*, 2016, DOI: 10.1039/C5AN02441B.

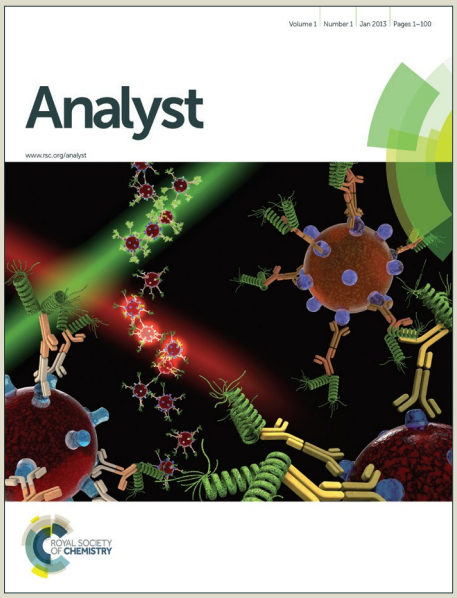

ROYAL SOCIETY OF CHEMISTRY

www.rsc.org/analyst

View Article Online
DOI: 10.1039/C5AN02441B

Journal Name

ARTICLE

Carbon Nanotubes Implanted Manganese-based MOFs for Simultaneous Detection of Biomolecules in Body Fluids

Min-Qiang Wang,[a] Cui Ye, [b] Shu-Juan Bao,* [a] Yan Zhang,[a] Ya-Nan Yu[a] and Mao-wen Xu,[a]

Metal-organic frameworks (MOFs) have recently attracted much interest in electrochemical fields due to their controlled porosity, large internal surface area, and countless structurally topologies. However, the direct application of single component MOFs is limited since they also exhibit poor electronic conductivity, low mechanical stability, and inferior electrocatalytic ability. To overcome these problems, we implanted multi-walled carbon nanotubes (MWCNTs) into manganese-based metal-organic frameworks (Mn-BDC) using a one-step solvothermal method and found that the introduction of MWCNTs can initiate the splitting of bulky Mn-BDC into thin layers. This splitting is highly significant in which it enhances the electronic conductivity and electrocatalytic ability of Mn-BDC. The constructed Mn-BDC@MWCNT composites were utilized as an electrode modifying material in the fabrication of an electrochemical sensor and then was used successfully for the determination of biomolecules in human body fluid. The sensor displayed successful detection performance with wide linear detection ranges (0.1~1150, 0.01~500, and 0.02~1100 μM for AA, DA and UA, respectively) and low limits of detection (0.01, 0.002, and 0.005 μM for AA, DA and UA, respectively); thus, this preliminary study presents an electrochemical biosensor constructed with novel electrode modifying material that exhibits superior potential for the practical detection of AA, DA and UA in urine samples.

Received 00th January 20xx,
Accepted 00th January 20xx

DOI: 10.1039/x0xx00000x

www.rsc.org/

1. Introduction

It is highly common for ascorbic acid (AA), dopamine (DA) and uric acid (UA) to coexist in biological fluids, such as serum and urine. AA is found in foods, plants, and animal tissues and takes part in important biological reactions, including immunity, free radical scavenging, and cancer prevention.[1] DA is an important neurotransmitter for message transfers in human metabolism as well as in the central nervous and renal systems.[2] Uric acid (UA), the primary end-product of purine metabolism, is another important biomolecule present in urine and blood; however, abnormal levels of UA can cause several diseases, including gout, hyperuricemia, and Lesch Nyan syndrome.[3] Therefore, detections of AA, DA and UA are crucial not only for biomedical chemistry and neurochemistry but also for diagnostic and pathological research. However, the simultaneous detection of AA, DA and UA using commercial conventional electrodes is highly difficult since these chemicals usually foul the electrodes, and their oxidation potentials easily overlap. In order to overcome these problems, various materials, such as Poly-Chromazurols[4], Fe_3O_4@Au composite (Fe_3O_4@Au-S-Fc)[5], pristine graphene (PG)[6], nitrogen-doped porous carbon nanopolyhedra (N-PCNPs)[7], rGO-supported porous alloyed Pd-Ag nanocomposites (Pd-Ag NFs/rGO)[8], and Pd-Pt nanoparticles anchored on reduced grapheme oxide with the aid of PDDA (Pd_3Pt_1/PDDA-RGO)[9], have been used to fabricate electrodes to enhance the sensitive and selective determination of these biomolecules. However, the linear detection range for the above-modified electrodes is not wide enough, and the performances are closely dependent on the electrode material. Hence, the discovery of novel and efficient modifying materials is still highly desired by researchers.

Metal-organic frameworks (MOFs) is an interesting class of porous solids constructed from a variety of molecular complexes. MOFs have drawn considerable attention due to their fascinating structures and potential applications in catalysis[10], drug release[11], gas separation[12], optoelectronics and energy storage[13], et al. Particularly, MOFs have been considered to be one of leading candidates for sensing materials due to their unique properties of crystalline ordered structures, tunable pore sizes, and high biocompatibility.[14] Wang et al. reported a hybrid nanocomposite of copper terephthalate MOF-graphene oxide and used it as an electrochemical sensing platform for the determination of acetaminophen (ACOP) and dopamine (DA).[15] However, the direct application of single component MOFs in electrochemistry is limited owing to their poor electronic conductivity, low mechanical stability, and inferior electrocatalytic ability. To overcome these disadvantages, various functional guest species have been introduced into MOF host matrices, which provide the opportunity to achieve desired properties and largely expanded MOF-based applications. Michal et al. infiltrated palladium into the highly

[a] Institute for Clean Energy & Advanced Materials, Faculty of Materials and Energy, Southwest University, Chongqing 400715, P.R. China. E-mail:baoshj@swu.edu.cn
[b] Key Laboratory of Luminescent and Real-Time Analytical Chemistry, Ministry of Education, College of Chemistry and Chemical Engineering, Southwest University, Chongqing 400715, P. R. China.

Electronic Supplementary Information (ESI) available: [details of any supplementary information available should be included here]. See DOI: 10.1039/x0xx00000x

View Article Online
DOI: 10.1039/C5AN02441B

porous metal-organic framework MOF-5.[16] Haruta et al. reported a variety of Au@MOF materials and their catalytic properties in the oxidation of alcohols.[17] Recently, due to their high conductance, tensile strength, chemical stability, and ultra-small size, carbon nanotubes (CNTs) have been incorporated as the filler to endow the composite coatings with functional properties.[18, 19] Moreover, chemical modification of CNTs is also an important endeavor and promising methodology for optimizing their properties in various applications. Several methods have been developed for the functionalization of CNTs during the last few years.[20] Therefore, the research in the development of combining new materials with the CNTs is of great significance.

In this preliminary study, we implanted carboxyl MWCNTs into a Mn-based metal-organic framework (Mn-BDC) using a one-step solvothermal method. Mn-based MOFs have high chemical and thermal stability due to strong Mn-O bonds and a compact structure, while their pores provide penetration channels for the transit of biomolecules.[21] Moreover, Mn-BDC is a very high biocompatibility material, and MWCNTs are excellent electrode materials due to their unique structure, good electrical conductivity, and mechanical strength. Based on the properties described above, Mn-MOFs and MWCNTs were selected as the raw materials to synthesize the Mn-BDC@MWCNT heterostructure for the simultaneous detection of AA, DA and UA. The sensing performance of the electrochemical sensor based on the Mn-BDC@MWCNT heterostructure was investigated. In this study, wide linearity ranges, high sensitivity, and low detection limits were acquired, which provides a new opportunity to design sensitive electrochemical sensors with superior anti-interference performance. Furthermore, the developed sensor was used for the determination of biomolecular compounds in human urine samples successfully.

2. Materials and methods

2.1 Materials

$Mn(NO_3)_2•6H_2O$ was purchased from Sinopharm Chemical Reagent Co., *p*-benzenedicarboxylic acid (PTA) and *N*,*N*-dimethylformamide (DMF) were purchased from Aladdin Industrial Co., (Shanghai, China). Multi-walled carbon nanotubes (MWCNTs), NaCl, Na_2SO_4 and $NaNO_3$ were purchased from Chengdu Organic Chemicals Co., (Chengdu, China). Ascorbic acid (AA), dopamine (DA) and uric acid (UA) were purchased from Sigma Chemical Co., glucose, glutamic acid, L-cysteine and citric acid were obtained from Aladdin Industrial Co., (Shanghai, China). Double-distilled water was used for all experiments. Phosphate buffered saline (PBS, 0.1 M) containing 0.15 M NaCl at different pH was prepared by mixing stock solutions of Na_2HPO_4 and NaH_2PO_4, and the pH was adjusted with H_3PO_4 and NaOH. All other reagents were of analytical grade and used without further purification.

2.2 Characterization techniques

The X-ray diffraction pattern (XRD) were obtained with a XRD-7000 (XRD, Shimadzu XRD-7000) with Cu Kα source radiation at a scanning rate of 2° min^{-1} from 5° to 60°. The morphology and microstructure of the samples were investigated by field-emission scanning electron microscopy (FESEM, JEOL-7800F) and transmission electron microscopy (TEM, JEM-2100). The composition of the synthesized materials was characterized by X-ray photoelectron spectroscopy (XPS, Escalab 250xi, Thermo Scientific). The Brunauer-Emmett-Teller (BET) surface area was measured by Quadrasorb evo 2QDS-MP-30 (Quantachrome Instruments, USA) using nitrogen as the adsorption gas. The Electrochemical measurements were carried out on a conventional three-electrode system with the as-prepared electrodes as the working electrode, a platinum wire as the counter electrode, and a saturated calomel electrode (SCE) as the reference electrode on a CHI660 electrochemical workstation (CHI Instruments Inc.).

2.3 The preparation of materials

Preparation of carboxyl MWCNTs. MWCNTs were dispersed in a mixed acid (including equal volume of concentrated sulphuric acid and concentrated nitric acid) for 12 h at 70°C in oil bath under stirring. The resultant solid was separated, washed with deionized water and dried under vacuum.

Synthesis of Mn-BDC and Mn-BDC@MWCNT composites. Mn-BDC nanocrystals were prepared according to the literature with some minor modification[21]. A dispersion of $Mn(NO_3)_2•6H_2O$ (0.25 g) in 15 mL alcohol was rapidly added to a dispersion of p-benzenedicarboxylic acid (PTA) (0.166 g) in 15 mL N,N-dimethylformamide (DMF). After stirring for 1 h, the mixture was then transformed into a Teflon-lined stainless steel autoclave with a capacity of 40 mL and heated to 180°C for 24 h. Finally, the resulting precipitate was washed with DMF and alcohol several times, and the product was dried at 60°C in a vacuum. The Mn-BDC@MWCNT composites were prepared under the same solvothermal procedures as above, except carboxyl multi-walled CNTs (15 mg) were well dispersed in deionized water by sonication prior to adding to the N,N-dimethylformamide (DMF) solution.

2.4 Preparation of modified electrodes

The glassy carbon electrode (GCE) was respectively polished with 0.3 and 0.05 μm alumina slurry followed by rinsing thoroughly with double distilled water, and then ultrasonically cleaned in ethanol and double distilled water to obtain a mirror-like surface. The as-prepared Mn-BDC@MWCNTs (5 μL, 2 $mg·ml^{-1}$) was dropped onto the well-polished bare GCE and then evaporated in air. Then, Nafion (5 μL, 2.5%) was dropped on the surface of Mn-BDC@MWCNTs composite to form a Nafion membrane (Mn-BDC@MWCNTs/GCE). Similar procedure was also applied to prepare Mn-BDC modified electrode (Mn-BDC /GCE) for a comparative study.

3. Results and discussion

3.1 Characterization of Mn-BDC@MWCNTs nanocomposites

Fig.1 provides the x-ray diffraction (XRD) patterns of the parent materials and composites of Mn-BDC@MWCNTs. There is good agreement between our obtained pattern of Mn-BDC and the one reported in the literature[21], demonstrating a successful synthesis procedure. The similar diffraction patterns of the composites to Mn-BDC indicate the existence of well-defined MOF units, proving

View Article Online
DOI: 10.1039/C5AN02441B

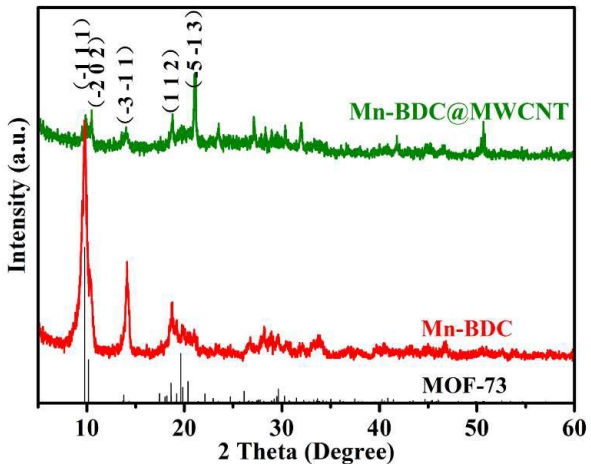

Fig. 1. Power x-ray diffraction patterns simulated from the x-ray crystal diffraction file for Mn-BDC, prepared Mn-BDC, and Mn-BDC@MWCNTs.

that MWCNTs did not prevent the formation of linkages between the manganese dimers and the organic bridges. However, a narrow peak with the highest intensity along the (-1 1 1) direction was observed in the XRD patterns of pure Mn-BDC, while a narrow peak with the highest intensity along the (-5 -1 3) direction was displayed in that of Mn-BDC@MWCNTs, which indicates that the MWCNTs have favorable minimum surface-free energy for oriented growth along the (-5 -1 3) direction[22]. This result may be caused by the change of density in nucleation centers at the time of crystal growth and in turn inducing the change of lattice strain of the crystals when the MWCNTs were introduced. It is interesting to note that the peak of MWCNTs was not found for the composites. One reason this may have occurred is because the peak of MWCNTs at 26° was overlapped by the relatively high intensity sharp peak of Mn-BDC, and the content of MWCNTs in the composites is relatively low (about 11 wt % judged by thermogravimetric analysis (TGA)). Another explanation is the ascribed high dispersion of MWCNTs due to the presence of polar solvents (particularly DMF), which are known to disperse MWCNTs very well.[23] Hence, the participation of MWCNTs in the reaction process has no influence on the formation of linkages between the manganese and the organic bridges. In addition, MWCNTs facilitate the crystal size distribution with non-uniformity and heterogeneity.

To examine the detailed nanostructure of the as-prepared materials, we further performed field emission scanning electron microscopy (FESEM) and transmission electron microscopy (TEM). As shown in Fig. 2(a), the pure Mn-BDC is very bulky. After introducing MWCNTs, the obtained Mn-BDC@MWCNT composite became looser compared to the original form (Fig. 2(b) and (c)) and split into thin layers, suggesting that the carboxyl MWCNTs play an important role in controlling the morphology of Mn-BDC. A ripening-splitting crystal-growth mechanism can be used to explain the splitting of Mn-BDC in the presence of MWCNTs. In the initial stage of the reaction, a large number of nuclei are formed on the surface of carboxyl MWCNTs through covalent bonds in a short time via the Ostwald-ripening process[24, 25], then a slow crystal growth follows. With the reaction proceeding, huge bulk starts to form, and a splitting process occurs at the same time[26]. The SEM and TEM images of Mn-BDC@MWCNTs in Fig 2(c) and (d) further

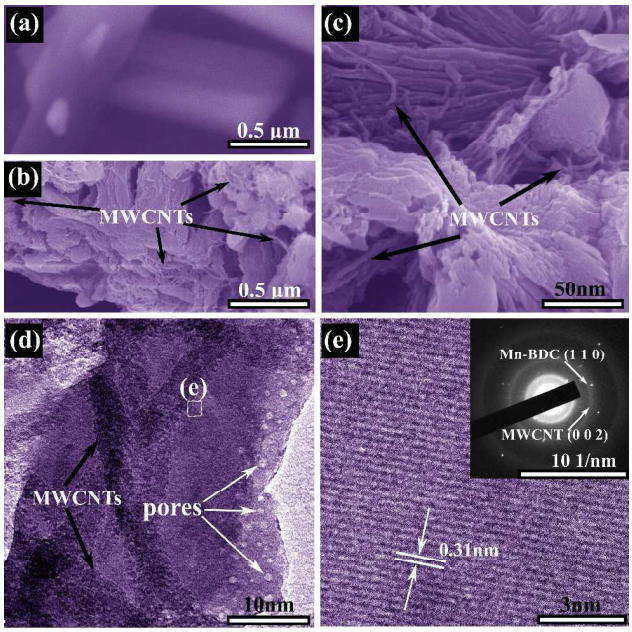

Fig.2 FESEM images at a low magnification of (a) pure Mn-BDC and (b) Mn-BDC@MWCNTs and (c) high magnification images of Mn-BDC@MWCNTs; (d) TEM images of Mn-BDC@MWCNT composites (white arrows represent the pores, and black arrows represent the MWCNTs on Mn-BDC@MWCNTs); (e) HRTEM image of Mn-BDC and inset shows selected area electronic diffraction (SAED) pattern of Mn-BDC@MWCNTs.

reveal that the MWCNTs retain their original morphology and have been implanted into Mn-BDC, where Mn-BDC with well-distributed pores was also observed. Fig. 2(e) shows the high resolution TEM (HRTEM) image of the square area in Fig. 2(d). The lattice fringe with an interplanar distance of 0.31 nm can be attributed to the (-4 -2 2) plane of Mn-BDC, while the corresponding selected area electron diffraction (SAED) pattern in the inset of Fig. 2(e) exhibits a single crystalline structure for the Mn-BDC and a polycrystalline for the MWCNTs

To evaluate the porosity of the materials, nitrogen adsorption measurements were carried out, and the isotherms were plotted in Fig. S1. Mn-BDC exhibited a type I isotherm, which indicates its predominant microporous character.[27] Compared to Mn-BDC, an obvious hysteresis loop was observed at a relative pressure of 0.8–1.0 P/P_0 for Mn-BDC@MWCNT composites, which might be ascribed to the presence of a mesoporous structure in the paralleled lamella of Mn-BDC or cavities of MWCNTs. Meanwhile, Mn-BDC@MWCNT composites have bigger Brunauer, Emmett and Teller (BET) surface area (112.72 m^2/g), pore volume, and pore radius than that of pure Mn-BDC (77.91 m^2/g) as show in table S1. Generally, the porosity of MOFs, which makes them particularly attractive, is often not fully utilized. The "incorporation" of MWCNTs in the composite was expected to prevent aggregation and favor the dispersion of nanosized MOF crystallites, which was confirmed by the HRTEM images. The increased mesoporous volumes and BET surface of Mn-BDC@MWCNT composites can be attributed to the slack and paralleled MOF lamellas, which improve the porosity and accessibility of the MOF network for adsorption.

View Article Online
DOI: 10.1039/C5AN02441B

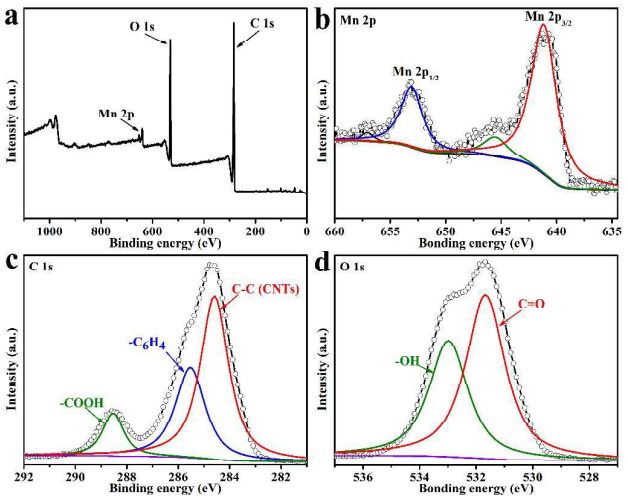

Fig.3 (a) Full-scan spectrum and (b-d) high resolution XPS spectra of the as-prepared Mn-BDC@MWCNT composites ((b) Mn 2p; (c) C 1s; and (d) O 1s regions).

X-ray photoelectron spectroscopy (XPS) was performed to characterize the Mn-BDC@MWCNT composite. The main peaks observed in the survey scan were $Mn2p_{3/2}$, $Mn2p_{1/2}$, C1s, and O1s centered at 653.1, 641.1, 284.5, and 531.2 eV, respectively (Fig. 3(a)). The Mn2p core level photoelectron spectrum displayed doublets for $Mn2p_{3/2}$ and $Mn2p_{1/2}$ at 641.1 and 653.1 eV respectively (Fig. 3(b)). The $Mn2p_{3/2}$ and $Mn2p_{1/2}$ main doublets were separated by ~12 eV. Similar satellite peaks were also observed for MnO, indicating that Mn in the synthesized MOF is divalent[21], which is consistent with that of the XRD result. The binding energy of the C1s emission peaks in Fig. 3(c) can be fitted quite well with one peak at 284.85 eV (MWCNTs) and two other peaks at 285.6 eV (TPA, phenyl carbons) and 289.7 eV (TPA, carbonyl carbons).[28] The binding energy of O1s can be decomposed into two contributions located at 533.1 eV and 531.7 eV (Fig. 3(d)). In accordance with earlier works, these two peaks are assigned to oxygen in the hydroxyl (–OH) and carbonyl (C=O) groups, respectively.[29] Conclusively, our results clearly demonstrate that the Mn-BDC@MWCNT composites were successfully synthesized.

3.2 Electrochemical activities of modified electrodes

The electrochemical properties of the modified electrodes were also investigated. Initially, the different electrodes werecharacterized using cyclic voltammetry (CV) in the presence of an external redox probe $[Fe(CN)_6]^{3-/4-}$ (Fig. 4(a)). Redox behavior of

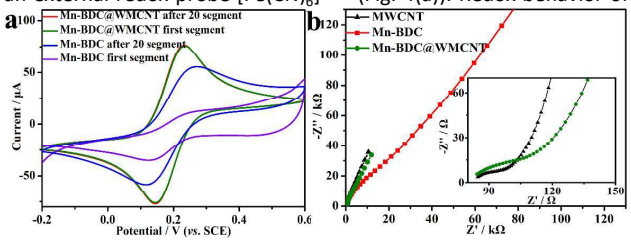

Fig.4 (a) CV curves of Mn-BDC/GCE and Mn-BDC@MWCNTs/GCE sensors at the first cycle and 20th cycle in a 5 mM $[Fe(CN)_6]^{3-/4-}$ mixture (1:1) containing 0.1 M KCl: scan rate, 0.1 Vs^{-1}. (b) EIS of MWCNTs/GCE, Mn-BDC/GCE, and Mn-BDC@MWCNTs/GCE in a 0.2 M $[Fe(CN)_6]^{3-/4-}$ mixture (1:1) containing 0.1 M KCl.

$[Fe(CN)_6]^{3-/4-}$ was observed on the Mn-BDC/GCE and Mn-BDC@MWCNTs/GCE sensors in a probe concentration of 5 mM. The peak current increased when MWCNTs were implanted into the Mn-BDC, indicating that the Mn-BDC@MWCNT composites facilitated fast electron transfer between the redox probe and electrode modifying materials. Furthermore, the Mn-BDC@MWCNT-modified electrode maintained about the same current as the original peak current and peak potential after 20 cycles, but the peak current and peak potential of the Mn-BDC-modified electrode increased with the augment of cycles, which indicated that the stability of Mn-BDC improved dramatically. Therefore, MWCNTs provide a channel for the electronic transmission in the nanocomposite and prevent the polarization of Mn-BDC.

Furthermore, electrochemical impedance spectroscopy (EIS) was performed for the different modified electrodes in $[Fe(CN)_6]^{3-/4-}$ to evaluate interfacial changes in the fabrication process of the biosensor. As shown in Fig. 4(b), the Mn-BDC/GCE sensor showed an approximately 45° line in the low-frequency region and an inconspicuous large arc in the high-frequency region. When the MWCNTs were implanted into Mn-BDC, a straight line in the low-frequency region was seen, and the diameter of the arc decreased significantly. This is indicative that Mn-BDC@MWCNT composites possess superior conductivity compared to the Mn-BDC materials, which may be accountable to superior conductivity and bigger pore size of the MWCNTs. Thereby, the electrochemical sensing platform was constructed as expected.

Differential pulse voltammetry (DPV) was used to evaluate the feasibility of Mn-BDC and Mn-BDC@MWCNT-modified electrodes for simultaneous determination of AA, DA and UA. Three well-defined and separate oxidation peaks were observed in Fig. 5(a). The separations between the peak potentials of AA-DA and DA-UA were 184 and 145 mV, respectively, in which the potential difference was large enough to determine these analytes individually or simultaneously. Moreover, the electrochemical stability of Mn-BDC/GCE and Mn-BDC@MWCNTs/GCE sensors were also investigated in our work. As seen in Fig. 5(a), when the concentration of analytes increased (from curve b to c), the peak potentials of Mn-BDC/GCE shifted right, but the peak potential of the Mn-BDC@MWCNTs/GCE electrode maintained its initial potential. This result may be due to the particle size of pure Mn-BDC, which is large, and the diffusion of analytes in Mn-BDC is limited, leading to the fact that oxidation of analytes only occurs on the surface the compound. Meanwhile, the poor conductivity of

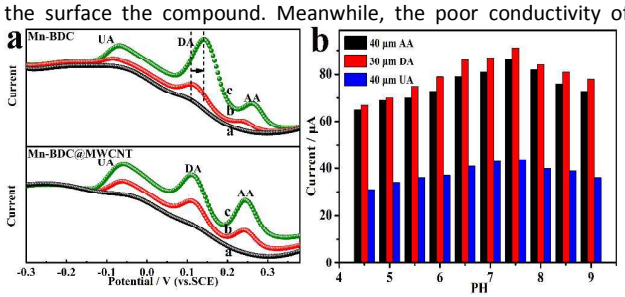

Fig.5 (a) Differential pulse voltammetry (DPV) responses of Mn-BDC/GCE and Mn-BDC@MWCNTs/GCE sensors in pH=7.5 buffer with various concentration of AA (0, 40, and 80 μM). DA (0, 20, and 40 μM), and UA (0, 40, and 80 μM). (b) Optimization of pH for the detection of 40 μM AA, 30 μM DA and 40 μM UA by the DPV method in pH of 7.5 buffer at a scan rate of 0.1 Vs^{-1}.

View Article Online
DOI: 10.1039/C5AN02441B

Mn-BDC resulted in the polarization of Mn-BDC/GCE via an electrocatalytic reaction process. In contrast, the Mn-BDC@MWCNT composites possess split, thin layers, a larger specific surface area, is more mesoporous, and has better conductivity, which are all confirmed above and provide excellent ion and electronic transfer channels for fast electrochemical reactions.

3.3 Optimization of pH

In order to achieve high sensitivity and selectivity, the pH buffer was optimized as shown in Fig. 5(b). It is clear that the DPV of the Mn-BDC@MWCNTs/GCE sensor shows a strong dependence on the solution's pH value. The peak current increases with increasing pH until the maximum peak current reaches pH=7.5. With further increase of pH, the peak current decreased gradually. For better compatibility in biological systems, a pH of 7.5 was chosen as the optimal value for subsequent electrochemical detection.

3.4 Individual and simultaneous determination of AA, DA and UA

Based on the CV and DPV results, simultaneous determinations of AA, DA and UA were achieved on the Mn-BDC@MWCNT-modified electrode with well-separated oxidation peak potentials. As shown in Fig. 6, the oxidation peak currents of analytes increased linearly with increasing concentration. The linear responses for the individual determination of AA(Fig. 6(a)), DA(Fig. 6(b)) and UA(Fig. 6(c)) were observed in the concentration ranges of 0.1–1150 μM, 0.01–500 μM, and 0.02–1100 μM with detection limits of 0.01 μM, 0.002 μM, and 0.005 μM (S/N=3), respectively. Compared to other published reports listed in Table S2, our Mn-BDC@MWCNTs/GCE sensor reveals a wider linear detection range and lower detection limits than those of many nanomaterial-based electrochemical sensors.[30]

Usually, AA, DA and UA coexist in biological samples, and the oxidation potentials of these species are very similar. As such, the interferences that occur while acquiring measurements should be excluded. DPV was adopted to investigate the electro-oxidation processes when the concentration of one species changed, while those of the other two substances were kept constant. For example, the peak current of AA increased linearly with an increase in AA concentration from 1 to 700 μM, while those of DA and UA remained almost unchanged. No obvious interference was observed for the determination of AA in the presence of DA and UA (Fig. 6(d)). DA (Fig. 6(e)) and UA (Fig. 6(f)) present similar results, and their corresponding linear concentration ranges were 0.5–660 μM and 0.05–1400 μM, respectively. The detection limits of AA, DA and UA were calculated to be 0.25, 0.015, and 0.02 μM (S/N=3), respectively. The performances of several kinds of modified electrodes reported in previous literature for simultaneous determination of AA, DA and UA are summarized in Table S2. Obviously, the Mn-BDC@MWCNT composites fabricated in our work prove to be a promising candidate for simultaneous determination of AA, DA and UA in their ternary mixture without cross interference.

The simultaneous determination of AA, DA and UA by the Mn-BDC@MWCNTs/GCE sensor is shown in Fig. 7. The DPV oxidation peak currents increased linearly with the increase of their concentrations. The linear responses of AA, DA and UA were obtained in the concentration ranges of 1–600 μM, 0.1–420 μM, and 0.1–600 μM with detection limits of 0.25 μM, 0.024 μM, and 0.023 μM, respectively. The relative standard deviations (RSD) for determining AA, DA and UA (n =10) were 2.1 %, 1.8 %, and 2.5 %,

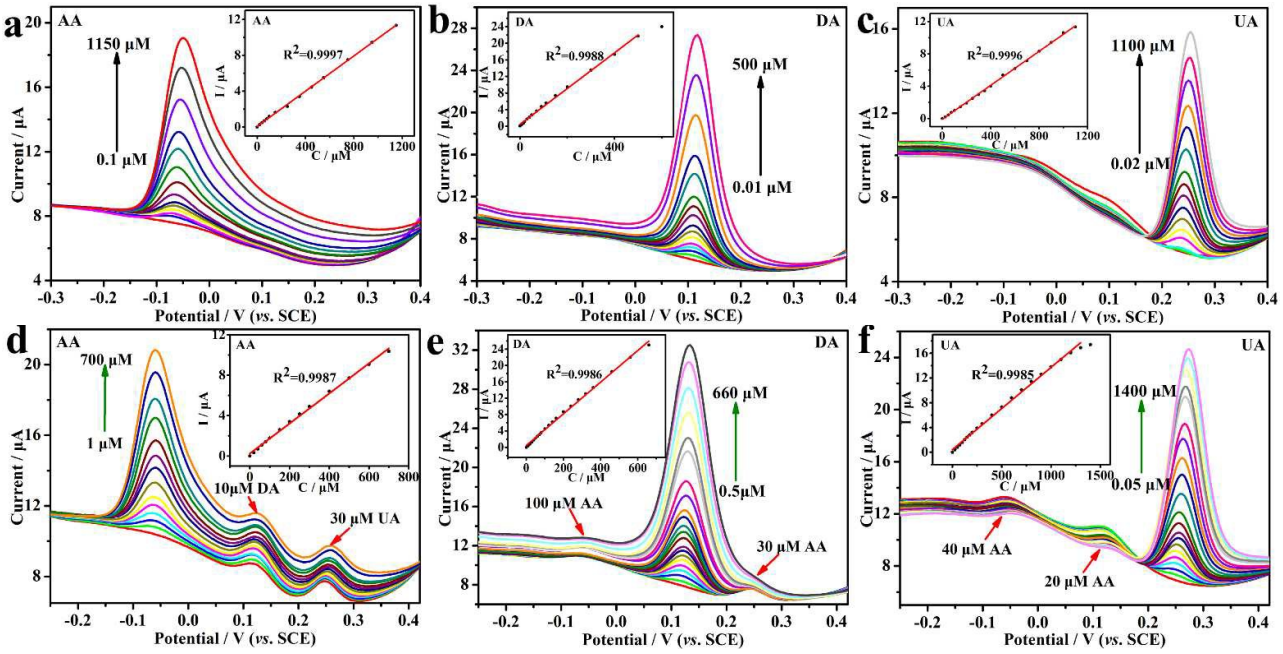

Fig.6 DPV responses of the Mn-BDC@MWCNTs/GCE sensor in pH of 7.5 buffer; (a) 0.1–1150 μM of AA; (b) 0.01–500 μM of DA; (c) and 0.02–1100 μM of UA; (d) containing 10 μM DA, 30 μM AA, and different concentrations of AA from 1–700 μM; (e) containing 100 μM AA, 30 μM UA, and different concentrations of DA from 0.05–660 μM; (f) containing 40 μM AA, 20 μM DA, and different concentrations of UA from 0.05–1400 μM. The inset shows the calibration curve between oxidation peak current and the concentration of AA, DA and UA.

View Article Online
DOI: 10.1039/C5AN02441B

Journal Name

ARTICLE

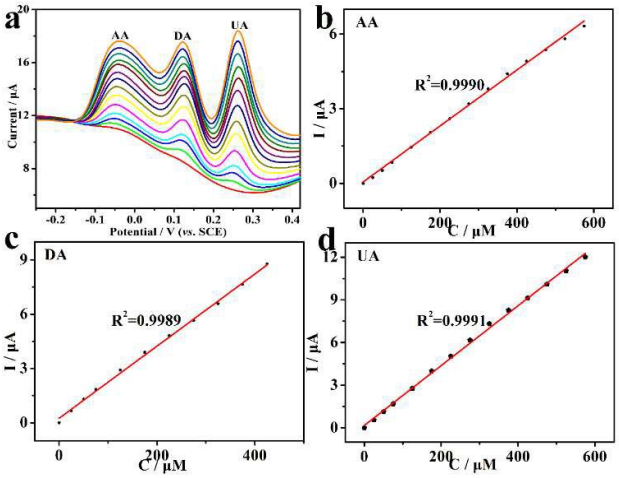

Fig.7 DPV responses at Mn-BDC@MWCNTs/GCE in pH=7.5 buffer with various concentrations of AA, DA and UA from 1–600 μM, 0.1–420 μM and 0.1–600 μM (a), calibration curve between oxidation peak current and the concentration of AA (b), DA(c), and UA(d).

respectively. These results demonstrate that simultaneous detection of these analytes was achieved on the Mn-BDC@MWCNTs/GCE sensor with high sensitivity and selectivity. Our sensors show lower detection limits and wider concentration ranges towards the oxidation of AA, DA and UA than those reported previously (Table S2) due to the excellent conductivity and catalytic activity of the Mn-BDC@MWCNT composites with unique porous construction. Therefore, the Mn-BDC@MWCNT composites, as an advanced electrode material, prove to exhibit promising application in electrochemical detection.

3.5 Stability and reproducibility of sensors

DPV responses were carried out to investigate the stability of our fabricated sensors. When the electrodes were stored at 4°C for ten days, the response currents of AA, DA and UA decreased by 4.12%, 3.84%, and 4.35%, respectively. The reproducibility of the developed sensor was also tested by DPV measurement using six different electrodes. The relative standard deviations (RSD) of the DPV response currents for the three species were less than 2.1%. These results show that the Mn-BDC@MWCNTs/GCE sensor possesses acceptable stability and reproducibility for analytical applications.

3.6 Practical applications

The anti-interference performance towards ions and other small molecules, which are possibly oxidized along with analyte molecules on the electrode surface to cause interfering electrochemical signals, is one of the biggest concerns for electrochemical sensors. Thus, it is essential to investigate the effects of interferences on the current response of the sensing materials for analyte oxidation. Fig. S3 shows the amperometric response obtained by successive additions (20 μM for each addition) of AA, DA and UA containing some possible interference in pH=7.5 buffer at the applied potentials of -0.09, 0.12, and 0.27 V. The response current of Cl^-, NO_3^-, SO_4^{2-}, glucose, glutamic acid, L-cysteine, and citric acid did not increase, suggesting that our sensors exhibited good selectivity for the determination of the three analytes.

The Mn-BDC@MWCNTs/GCE sensor was also applied to analyze urine using the standard addition method. All of the urine samples were diluted 30 times with pH=7.5 buffer, and the determination of each sample was performed using DPV. The results are presented in Table S3 and indicate that the Mn-BDC@MWCNTs/GCE sensor is effectively used for the determination of AA, DA and UA in real urine samples.

4. Conclusions

In summary, we present a preliminary study of implanting MWCNTs into Mn-BDC using a one-step solvothermal method. The obtained Mn-BDC@MWCNTs composites possess porous slack structure, large specific surface area, high conductivity, and excellent electrocatalytic activity. A novel electrochemical biosensor was fabricated using Mn-BDC@MWCNTs, which exhibits wider concentration ranges and lower detection limits for simultaneous detection of AA, DA and UA with good selectivity and sensitivity. The prepared sensor also shows excellent stability and repeatability and was applied effectively to the determination of AA, DA and UA in spiked samples of human urine. Thus, the proposed method provides a promising strategy for the simultaneous detection of DA AA, and UA in biological samples.

Acknowledgements

This work is financially supported by National Natural Science Foundation of China (21163021, 31200700, 21375108); Chongqing Key Laboratory for Advanced Materials and Technologies of Clean Energies; Natural Science Foundation of Chongqing (cstc2013jcyjA5004) and Program for Excellent Talents in Chongqing (102060-20600218).

References

1 Yang, F.; Wang, J.; Cao, Y.; Zhang, L.; Zhang, X. *Sens Actuators B* 2014, 20–25.
2 Yuan, D.; Chen, S.; Yuan, R.; Zhang, J.; Liu, X. *Sens Actuators B* 2014, *191*, 415-420.

View Article Online
DOI: 10.1039/C5AN02441B

3 Wang, C.; Yuan, R.; Chai, Y.; Chen, S.; Hu, F.; Zhang, M. *Anal Chim Acta* 2012, *741*, 15–20.
4 Taei, M.; Shafizadeh, A.; Fouladgar, M.; Hasanpour, F. *J Appl Chem* 2013, *7*, 116-130.
5 Liu, M.; Chen, Q.; Lai, C.; Zhang, Y.; Deng, J.; Li, H.; Yao, S. *Biosens Bioelectron* 2013, *48*, 75-81.
6 Qi, S.; Zhao, B.; Tang, H.; Jiang, X. *Electrochim Acta* 2015, 395–402.
7 Gai, P.; Zhang, H.; Zhang, Y.; Liu, W.; Zhu, G.; Zhang, X.; Chen, J. *J Mater Chem B* 2013, *1* , 2742-2749.
8 Chen, L. X.; Zheng, J. N.; Wang, A. J.; Wu, L. J.; Chen, J. R.; Feng, J. J. *Analyst* 2015, *140*, 3183-3192.
9 Yan, J.; Liu, S.; Zhang, Z.; He, G.; Zhou, P.; Liang, H.; Tian, L.; Zhou, X.; Jiang, H. *Colloids and Surf., B* 2013, *111*, 392-397.
10 Xu, M.; Han, J.-M.; Wang, C.; Yang, X.; Pei, J.; Zang, L. *Appl Mater Inter* 2014, *6*, 8708-8714.
11 Tan, L. L.; Li, H.; Zhou, Y.; Zhang, Y.; Feng, X.; Wang, B.; Yang, Y. W. *Small* 2015, 31, 3807-3714..
12 Burmann, P.; Zornoza, B.; Téllez, C.; Coronas, J. *Chem Eng Sci* 2014, *107*, 66–75.
13 Zhang, J.; Li, F.; Schick, C.; Liu, S.; Sun, L.; Xu, F.; Jiao, C.; Li, Z.; Wang, S.; Wang, Z. *Energy Environ Sci* 2013, *6*, 818-823.
14. Hanke, M.; Arslan, H. K.; Bauer, S.; Zybaylo, O.; Christophis, C.; Gliemann, H.; Rosenhahn, A.; Woll, C. *Langmuir* 2012, *28* , 6877-84.
15 Wang, X.; Wang, Q.; Wang, Q.; Gao, F.; Gao, F.; Yang, Y.; Guo, H. *Appl Mater Inter* 2014, *6* , 11573-11580.
16 Sabo, M.; Henschel, A.; Fröde, H.; Klemm, E.; Kaskel, S. *J Mater Chem* 2007, *17* , 3827-3832.
17 Ishida, T.; Nagaoka, M.; Akita, T.; Haruta, M. *Chem* 2008, *14*, 8456-8460.
18 Tang, Q.; Chen, M.; Yang, C.; Wang, W.; Bao, H.; Wang, G. *Appl. Mater. Inter* 2015, *7*, 103-15313.
19 Li, S.; Zhao, Z.; Huang, Y.; Di, J.; Jia, Y.; Zheng, H. *J.mater.chem.a* 2015, *3*, 5467-5473.
20 Datsyuk, V.; Kalyva, M.; Papagelis, K.; Parthenios, J.; Tasis, D.; Siokou, A.; Kallitsis, I.; Galiotis, C. *Carbon* 2008, *46*, 833–840.
21 NL, R.; J, K.; M, E.; B, C.; M, O. K.; OM, Y. *J Amer Chem Soc* 2005, *127*, 1504-1518.
22 Joseph, D., Paul; Saravanan, M.; Muthuraaman, B., Renugambal, P., Sambasivam, S., Raja, S., Philip; Maruthamuthu, P., Venkateswaran, C. *Nanotech* 2008, *19*, 19158-19161.
23 Prasad, R.; Bhat, B. R. *Sens Actuators B* 2015, *220*, 81–90.
24 Tang, Z.; Wang, Y.; Shanbhag, S.; Giersig, M.; Kotov, N. A. *J Amer Chem* 2006, *128*, 6730-6736.
25 Ju, Z.; Zhang, E.; Zhao, Y.; Xing, Z.; Zhuang, Q.; Qiang, Y.; Qian, Y. *Small* 2015, 11, 4753-4761
26 Bao, S. J.; Bao, Q. L.; Li, C. M.; Chen, T. P.; Sun, C. Q.; Dong, Z. L.; Gan, Y.; Zhang, J. *Small* 2007, *3*, 1174-1177.
27 Xu, M.; Kong, L.; Zhou, W.; Li, H. *J Phy Chem C* 2007, *111*, 19141-19147.
28 Zhang, W.; Nefedov, A.; Naboka, M.; Cao, L.; C, W. L. *Phys.Chem.* 2012, *14*, 10125-10131.
29 M.Wuhn; J.Weckesser; Ch.Woll. *Langmuir* 2001, *17*, 7605-7612.
30 Filik, H.; Avan, A. A. h.; Aydar, S. *Arab J of Chem 2015, 8*. DOI: 10.1016/j.arabjc.2015.01.014